

**Microscopic description of octupole collective excitations near  $N = 56$  and  $N = 88$** K. Nomura<sup>1,\*</sup>, L. Lotina,<sup>1</sup> T. Nikšić,<sup>1</sup> and D. Vretenar<sup>1,2</sup><sup>1</sup>*Department of Physics, Faculty of Science, University of Zagreb, HR-10000 Zagreb, Croatia*<sup>2</sup>*State Key Laboratory of Nuclear Physics and Technology, School of Physics, Peking University, Beijing 100871, China*

(Received 8 January 2021; accepted 16 April 2021; published 3 May 2021)

Octupole deformations and related collective excitations are analyzed using the framework of nuclear density functional theory. Axially symmetric quadrupole-octupole constrained self-consistent mean-field (SCMF) calculations with a choice of universal energy density functional and a pairing interaction are performed for Xe, Ba, and Ce isotopes from proton-rich to neutron-rich regions, and neutron-rich Se, Kr, and Sr isotopes, in which enhanced octupole correlations are expected to occur. Low-energy positive- and negative-parity spectra and transition strengths are computed by solving the quadrupole-octupole collective Hamiltonian, with the inertia parameters and collective potential determined by the constrained SCMF calculations. Octupole-deformed equilibrium states are found in the potential energy surfaces of the Ba and Ce isotopes with  $N \approx 56$  and 88. The evolution of spectroscopic properties indicates enhanced octupole correlations in the regions corresponding to  $N \approx Z \approx 56$ ,  $Z \approx 88$  and  $Z \approx 56$ , and  $N \approx 56$  and  $Z \approx 34$ . The average  $\beta_{30}$  deformation parameter and its fluctuation exhibit signatures of octupole shape-phase transition around  $N = 56$  and 88.

DOI: [10.1103/PhysRevC.103.054301](https://doi.org/10.1103/PhysRevC.103.054301)**I. INTRODUCTION**

The intrinsic shapes of most medium-heavy and heavy nuclei are characterized by reflection-symmetric, quadrupole deformations. Reflection-asymmetric or octupole deformations occur in specific mass regions with the proton  $Z$  and neutron numbers  $N$  near 34, 56, 88, and 134 [1,2]. Octupole correlations determine the systematics of low-lying negative-parity states, which form approximate alternating-parity doublets with the positive-parity ground-state bands, and the electric dipole and octupole transition strengths. The exploration of stable octupole deformations is a very active research field in both experimental and theoretical low-energy nuclear physics. In recent years, experiments with radioactive ion beams have identified octupole-deformed nuclei, e.g., in light actinides ( $^{220}\text{Rn}$ ,  $^{222,224,228}\text{Ra}$ , and  $^{228}\text{Th}$ ) [3–5] and lanthanides ( $^{144,146}\text{Ba}$ ) [6,7]. Experimental studies of octupole deformations have also been reported in lighter mass regions, e.g., the neutron-deficient nuclei with  $N \approx Z \approx 56$  [8–12], and neutron-rich nuclei with  $N \approx 56$  and  $Z \approx 34$  [13,14].

Theoretical analyses of octupole deformations have used a variety of nuclear structure models, such as the self-consistent mean-field (SCMF) methods [15–19], the interacting boson model (IBM) [20–24], the geometric collective model [25,26], and the cluster model [27,28]. Most of these studies have been focused on the regions corresponding to  $Z \approx 88$  and  $N \approx 134$ , and  $Z \approx 56$  and  $N \approx 88$ . However, octupole correlations in nuclei with particle numbers close to 34 and/or 56 have not been analyzed in much detail. A possible reason is that, especially because the  $N \approx Z \approx 56$  nuclei are close to

the proton drip line, experimental information is insufficient. Few exceptions are perhaps the Nilsson-Strutinsky calculation based on the Woods-Saxon potential in Refs. [15,29], the constrained Hartree-Fock+BCS calculation with the Skyrme force [30] of the light Xe and Ba isotopes in Ref. [31], and the global analysis of ground-state octupole deformation within the nuclear density functional theory (DFT) in Ref. [19]. However, in those studies calculations were carried out at the mean-field level or only for restricted spectroscopic properties. Because of renewed experimental interest in octupole shapes in extended mass regions, it is meaningful to carry out a new theoretical analysis of octupole deformations and related spectroscopy that also includes the lighter mass region with  $N/Z \approx 34$  and 56.

Nuclear DFT provides an accurate and economic microscopic approach to nuclear structure that enables systematic studies [32,33]. Both relativistic [34,35] and nonrelativistic [32,36] energy density functionals (EDFs) have successfully been applied in the global description of the ground-state properties and collective excitations. The basic implementation is in terms of SCMF calculations that produce energy surfaces as functions of shape and/or pairing collective variables. To compute spectroscopic properties, the SCMF framework must be extended to include dynamical correlations that arise from the restoration of broken symmetries and fluctuations around the mean-field minima. A straightforward approach is the generator coordinate method (GCM) [37] with symmetry projections and configuration mixing included. The GCM has been employed to study octupole correlations with axial quadrupole and octupole deformations as collective coordinates [38–43]. In practical applications to medium-heavy and heavy nuclei, however, the GCM is computationally challenging, especially as the number of nucleons or

\*knomura@phy.hr

collective coordinates increases. Alternative approaches to GCM have thus been developed, such as the quadrupole-octupole collective Hamiltonian (QOCH) [16,44,45] and the mapped *sdf*-IBM [23,24].

Based on the fully microscopic framework of nuclear DFT, here we carry out a systematic analysis of octupole collective excitations in the mass  $A \approx 90$ –150 regions: Xe, Ba, and Ce isotopes extending from proton-rich ( $N \approx Z \approx 56$ ) to neutron-rich ( $N \approx 88$  and  $Z \approx 56$ ) nuclei, and the neutron-rich Se, Kr, and Sr nuclei with  $Z \approx 34$  and  $N \approx 56$ . The starting points are axially symmetric quadrupole-octupole constrained SCMF calculations using the relativistic Hartree-Bogoliubov model with the density-dependent point-coupling (DD-PC1) [46] EDF, and a separable pairing force [47]. The relevant excitation spectra and transition rates are computed by solving the collective Schrödinger equation with the axially symmetric quadrupole  $\beta_2$  and octupole  $\beta_3$  shape degrees of freedom. The constrained SCMF calculations completely determine the moment of inertia, three mass parameters, and collective potential of the QOCH. The diagonalization of the QOCH yields the positive- and negative-parity excitation spectra, as well as the electric quadrupole, octupole, and dipole transition rates. We note that a similar SCMF+QOCH spectroscopic calculation, based on the PC-PK1 [48] EDF, was performed for a large number of medium-heavy and heavy nuclei: from Rn to Fm, and from Xe to Gd isotopes [16].

Here we further mention recent EDF-based beyond SCMF calculations of the octupole-related properties of nuclei. These include studies of, for instance, the global systematics of octupole correlations in the ground and excited states of virtually all even-even nuclei within the parity-projected GCM approach using the Gogny EDFs [49,50], and the onset of octupole deformations and related spectroscopy in neutron-rich Ba isotopes within the symmetry conserving configuration mixing calculations with the Gogny-D1S EDF [40,41], and within the multireference covariant energy density functional theory [42] with projections onto angular momentum, particle numbers, and parity.

This paper is organized as follows. In Sec. II we briefly review the formalism of the relativistic Hartree-Bogoliubov (RHB)+QOCH model. The SCMF  $\beta_2$ - $\beta_3$  potential energy surfaces are discussed in Sec. III. In Sec. IV the systematics of spectroscopic properties, including excitation energies of low-lying positive- and negative-parity states, and electromagnetic transition rates, are compared to available experimental data. The results for the  $N = 56$  isotones are presented in Sec. V. Signatures of octupole shape-phase transitions are examined in Sec. VI. Finally, a brief summary and conclusion are given in Sec. VII.

## II. THEORETICAL FRAMEWORK

### A. Relativistic Hartree-Bogoliubov calculation

The first step of the analysis is a set of constrained SCMF calculations of potential energy surfaces (PESs), performed using the RHB method [34] with the DD-PC1 [46] functional for the particle-hole channel, and a separable pairing force

of finite range [47] in the particle-particle channel. The constraints imposed in the SCMF calculations are the expectation values of the axially symmetric quadrupole  $Q_{20}$  and octupole  $Q_{30}$  moments:

$$\hat{Q}_{20} = 2z^2 - x^2 - y^2, \quad (1)$$

$$\hat{Q}_{30} = 2z^3 - 3z(x^2 + y^2). \quad (2)$$

The corresponding quadrupole and octupole deformation parameters  $\beta_2$  and  $\beta_3$  are defined by the relations

$$\beta_2 = \frac{\sqrt{5\pi}}{3r_0^2 A^{5/3}} \langle \hat{Q}_{20} \rangle, \quad (3)$$

$$\beta_3 = \frac{\sqrt{7\pi}}{3r_0^3 A^2} \langle \hat{Q}_{30} \rangle, \quad (4)$$

where  $r_0 = 1.2$  fm. The calculations are performed in a harmonic oscillator (HO) basis with the number of oscillator shells  $N_f = 10$  for the region  $Z \approx 34$  and  $N \approx 56$ . For heavier nuclei with  $Z \approx 56$  and  $N \geq 56$  a larger basis with  $N_f = 12$  is used.

### B. Quadrupole-octupole collective Hamiltonian

Collective states are described using an axially symmetric QOCH, with deformation-dependent parameters determined microscopically by the constrained RHB calculation. The QOCH contains the vibrational and rotational kinetic terms, and the collective potential

$$\hat{H}_{\text{coll}} = \mathcal{T}_{\text{vib}} + \mathcal{T}_{\text{rot}} + V_{\text{coll}}, \quad (5)$$

where the vibrational kinetic energy is parametrized by the mass parameters  $B_{22}$ ,  $B_{23}$ , and  $B_{33}$ ,

$$\mathcal{T}_{\text{vib}} = \frac{1}{2} B_{22} \dot{\beta}_2^2 + B_{23} \dot{\beta}_2 \dot{\beta}_3 + \frac{1}{2} B_{33} \dot{\beta}_3^2, \quad (6)$$

and the three moments of inertia  $\mathcal{I}_k$  determine the rotational kinetic energy,

$$\mathcal{T}_{\text{rot}} = \frac{1}{2} \sum_{k=1}^3 \mathcal{I}_k \omega_k^2. \quad (7)$$

Finally, the collective potential  $V_{\text{coll}}$  includes zero-point energy (ZPE) corrections. After quantization the collective Hamiltonian reads

$$\begin{aligned} \hat{H}_{\text{coll}} = & -\frac{\hbar^2}{2\sqrt{\omega\mathcal{I}}} \left[ \frac{\partial}{\partial \beta_2} \sqrt{\frac{\mathcal{I}}{\omega}} B_{33} \frac{\partial}{\partial \beta_2} - \frac{\partial}{\partial \beta_2} \sqrt{\frac{\mathcal{I}}{\omega}} B_{23} \frac{\partial}{\partial \beta_3} \right. \\ & \left. - \frac{\partial}{\partial \beta_3} \sqrt{\frac{\mathcal{I}}{\omega}} B_{23} \frac{\partial}{\partial \beta_2} + \frac{\partial}{\partial \beta_3} \sqrt{\frac{\mathcal{I}}{\omega}} B_{22} \frac{\partial}{\partial \beta_3} \right] \\ & + \frac{\mathcal{J}^2}{2\mathcal{I}} + V_{\text{coll}}(\beta_2, \beta_3), \end{aligned} \quad (8)$$

where  $\omega = B_{22}B_{33} - B_{23}^2$ . The mass parameters, moments of inertia, and collective potentials as functions of the collective coordinates  $(\beta_2, \beta_3)$ , are specified by the deformation-constrained self-consistent RHB calculations for a specific choice of the nuclear energy density functional and pairing interaction. In the present version of the model, the mass parameters defined as the inverse of the mass tensor,

$B_{ij}(\mathbf{q}) = \mathcal{M}_{ij}^{-1}(\mathbf{q})$ , are calculated in the perturbative cranking approximation

$$\mathcal{M}^{C_p} = \hbar^2 M_{(1)}^{-1} M_{(3)} M_{(1)}^{-1}, \quad (9)$$

where

$$[M_{(k)}]_{ij} = \sum_{\mu\nu} \frac{\langle 0 | \hat{Q}_i | \mu\nu \rangle \langle \mu\nu | \hat{Q}_j | 0 \rangle}{(E_\mu + E_\nu)^k}. \quad (10)$$

$|\mu\nu\rangle$  are two-quasiparticle wave functions, and  $E_\mu$  and  $E_\nu$  the corresponding quasiparticle energies.  $\hat{Q}_i$  denotes the multipole operators that correspond to the collective degrees of freedom. The collective potential  $V_{\text{coll}}$  is obtained by subtracting the vibrational ZPE from the total RHB deformation energy:

$$E_{\text{ZPE}} = \frac{1}{4} \text{Tr}[M_{(2)}^{-1} M_{(1)}]. \quad (11)$$

The microscopic self-consistent solutions of the constrained RHB equations, that is, the single-quasiparticle energies and wave functions on the entire energy surface as functions of the deformations, provide the microscopic input for the calculation of both the collective inertia and zero-point energy. The Inglis-Belyaev formula is used for the rotational moment of inertia. From the diagonalization of the collective Hamiltonian (5) one obtains the collective energy spectrum and eigenfunction. The eigenfunctions are expanded in terms of a complete set of basis functions. For each value of the angular momentum  $I$ , the basis is defined as

$$|n_2 n_3 IMK\rangle = (\omega\mathcal{I})^{-1/4} \phi_{n_2}(\beta_2) \phi_{n_3}(\beta_3) |IMK\rangle, \quad (12)$$

where  $\phi_{n_i}$  denotes the one-dimensional HO functions of  $\beta_{\lambda}$ . For positive-parity (negative-parity) states,  $n_3$  and  $I$  take even (odd) numbers. For axially symmetric shapes, the intrinsic projection of the total angular momentum  $K = 0$ . The collective wave function is then expressed as

$$\Psi_\alpha^{IM\pi}(\beta_2, \beta_3, \Omega) = \psi_\alpha^{I\pi}(\beta_2, \beta_3) |IM0\rangle, \quad (13)$$

with  $\Omega$  representing three Euler angles. The corresponding probability density distribution is defined as

$$\rho_\alpha^{I\pi}(\beta_2, \beta_3) = \sqrt{\omega\mathcal{I}} |\psi_\alpha^{I\pi}(\beta_2, \beta_3)|^2, \quad (14)$$

with the normalization

$$\int \rho_\alpha^{I\pi}(\beta_2, \beta_3) d\beta_2 d\beta_3 = 1. \quad (15)$$

The reduced transition probabilities  $B(E\lambda)$  are calculated from the relation

$$\begin{aligned} B(E\lambda; I_i \rightarrow I_f) \\ = (I_i 0 \lambda 0 | I_f 0)^2 \left| \int d\beta_2 d\beta_3 \sqrt{\omega\mathcal{I}} \psi_i \mathcal{M}_{E\lambda}(\beta_2, \beta_3) \psi_f^* \right|^2, \end{aligned} \quad (16)$$

where  $\mathcal{M}_{E\lambda}(\beta_2, \beta_3)$  is the electric moment of order  $\lambda$ , and the factor in parentheses on the right-hand side of the above expression is the Clebsch-Gordan coefficient. The electric moment is calculated as  $\langle \Phi(\beta_2, \beta_3) | \mathcal{M}_{E\lambda} | \Phi(\beta_2, \beta_3) \rangle$ , with  $\Phi(\beta_2, \beta_3)$  representing the wave functions obtained from the

RHB calculations. The corresponding operators  $\hat{\mathcal{M}}_{E\lambda}$  for dipole, quadrupole, and octupole transitions read

$$D_1 = \sqrt{\frac{3}{4\pi}} e \left( \frac{N}{A} z_p - \frac{Z}{A} z_n \right), \quad (17)$$

$$Q_2^p = \sqrt{\frac{5}{16\pi}} e (2z_p^2 - x_p^2 - y_p^2), \quad (18)$$

$$Q_3^p = \sqrt{\frac{7}{16\pi}} e (2z_p^3 - 3z_p(x_p^2 + y_p^2)), \quad (19)$$

respectively, where bare electric charge  $e$  is used, and this means no effective charges need to be introduced to calculate electromagnetic transition rates.

### III. SCMF RESULTS

#### A. Neutron-deficient $Z \approx 56$ nuclei

The axially symmetric ( $\beta_2, \beta_3$ ) PESs for neutron-deficient nuclei  $^{108-118}\text{Xe}$ ,  $^{110-120}\text{Ba}$ , and  $^{112-122}\text{Ce}$  are depicted in Fig. 1. Already at the most neutron-deficient isotopes with  $N = 54$ , the potential is considerably soft in  $\beta_3$  deformation, even though the minimum is on the  $\beta_3 = 0$  axis. Octupole-deformed equilibrium states with  $\beta_3 \neq 0$  occur in the  $N \approx Z$  nuclei  $^{112,114}\text{Ba}$  and  $^{114}\text{Ce}$ . There is no stable octupole-deformed minimum for the neighboring Xe isotopes, but the potential exhibits a narrow valley on the prolate side ( $\beta_2 > 0$ ) that is soft over a range of  $\beta_3$  values. Previous mean-field calculations have also suggested there are a few  $N \approx Z \approx 56$  nuclei that exhibit octupole-deformed equilibrium states on the potential energy surfaces [17,19,29,31]. For  $N > 64$ , not shown in the figure, the potential becomes rather softer in the  $\beta_2$  direction and the prolate deformation becomes larger around the middle of the major shell  $N = 66$ , but no octupole minima are found on the corresponding SCMF PESs. When approaching the neutron shell closure at  $N = 82$ , nearly spherical global minima are obtained with both the  $\beta_2$  and  $\beta_3$  deformations converging to zero.

#### B. Neutron-rich $Z \approx 56$ nuclei

Figure 2 displays the ( $\beta_2, \beta_3$ ) PESs for the isotopes  $^{140-150}\text{Xe}$ ,  $^{142-152}\text{Ba}$ , and  $^{144-154}\text{Ce}$  beyond the  $N = 82$  neutron shell closure. These neutron-rich isotopes are close to the empirical octupole magic number  $N = 88$ , and more extensive experimental and theoretical studies have been reported in this region compared to the neutron-deficient one with  $N \approx Z \approx 56$ . In all three isotopic chains the potential surfaces shown in Fig. 2 are more rigid in  $\beta_2$ , and pronounced octupole correlations are predicted. In particular, a number of neutron-rich Ba and Ce nuclei exhibit octupole-deformed global minima with nonzero value of  $\beta_3$ , that is, the isotopes  $^{144-152}\text{Ba}$  and  $^{146-152}\text{Ce}$ . The most pronounced octupole global minimum is found in nuclei with  $N \approx 88$ , in agreement with experimental findings. The  $\beta_2$ - $\beta_3$  PESs obtained in the present analysis for the neutron-rich lanthanides are also consistent with many of the recent SCMF calculations using both relativistic [16,17,24,42] and nonrelativistic EDFs [19,40,41].

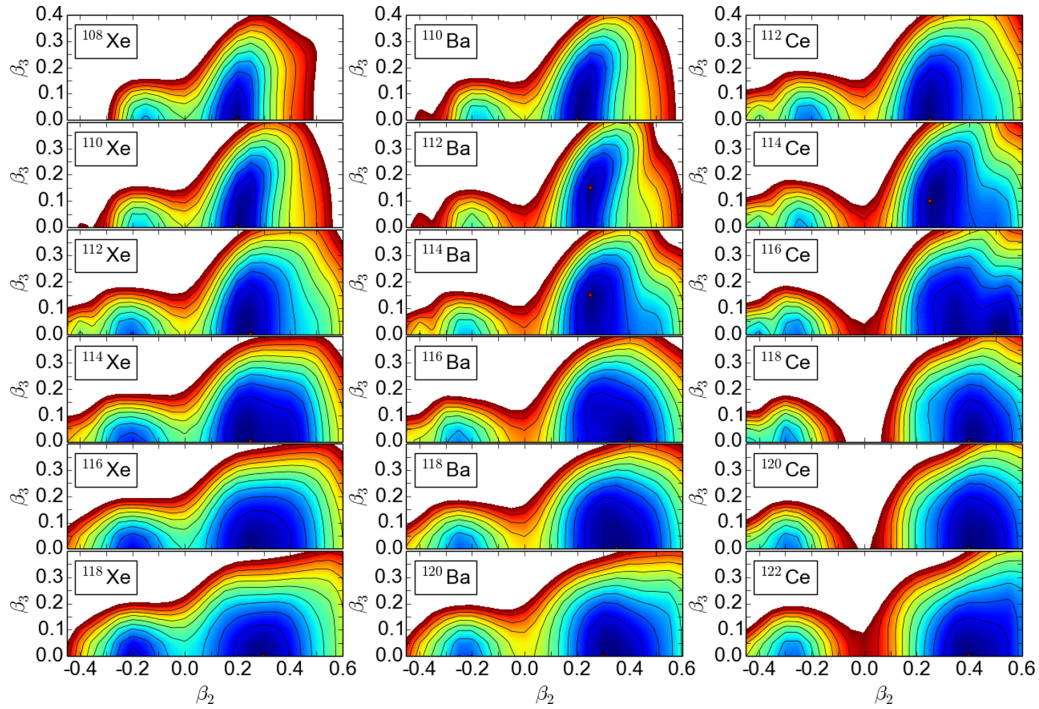


FIG. 1. SCMF ( $\beta_2, \beta_3$ ) PESs for  $^{108-118}\text{Xe}$ ,  $^{110-120}\text{Ba}$ , and  $^{112-122}\text{Ce}$ . Global minima are identified by the red dots. Contours join points on the surface with the same energy, and the difference between neighboring contours is 1 MeV.

### C. $Z \approx 34$ nuclei around $N = 56$

We also explore another mass region in which octupole correlations could develop. In Fig. 3 we plot the SCMF  $\beta_2$ - $\beta_3$  PESs for the neutron-rich nuclei  $^{86-96}\text{Se}$ ,  $^{88-98}\text{Kr}$ , and  $^{90-100}\text{Sr}$ , close to the proton  $Z = 34$  and neutron  $N = 56$  octupole

magic numbers. Even though octupole correlations are empirically expected to occur at proton number  $Z = 34$ , the PESs in the figure do not exhibit octupole global minima for these nuclei. In general, the  $(\beta_2, \beta_3)$  PESs for the  $Z \approx 34$  neutron-rich nuclei appear rather soft in  $\beta_2$  deformation. Taking as

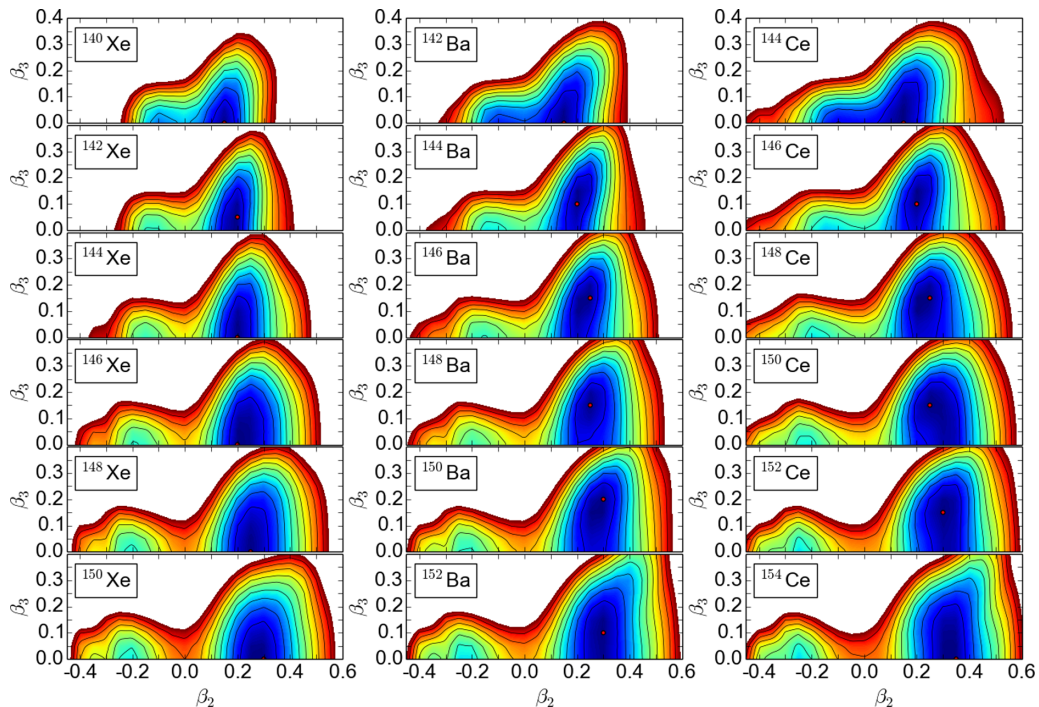


FIG. 2. Same as in the caption to Fig. 1 but for  $^{140-150}\text{Xe}$ ,  $^{142-152}\text{Ba}$ , and  $^{144-154}\text{Ce}$ .

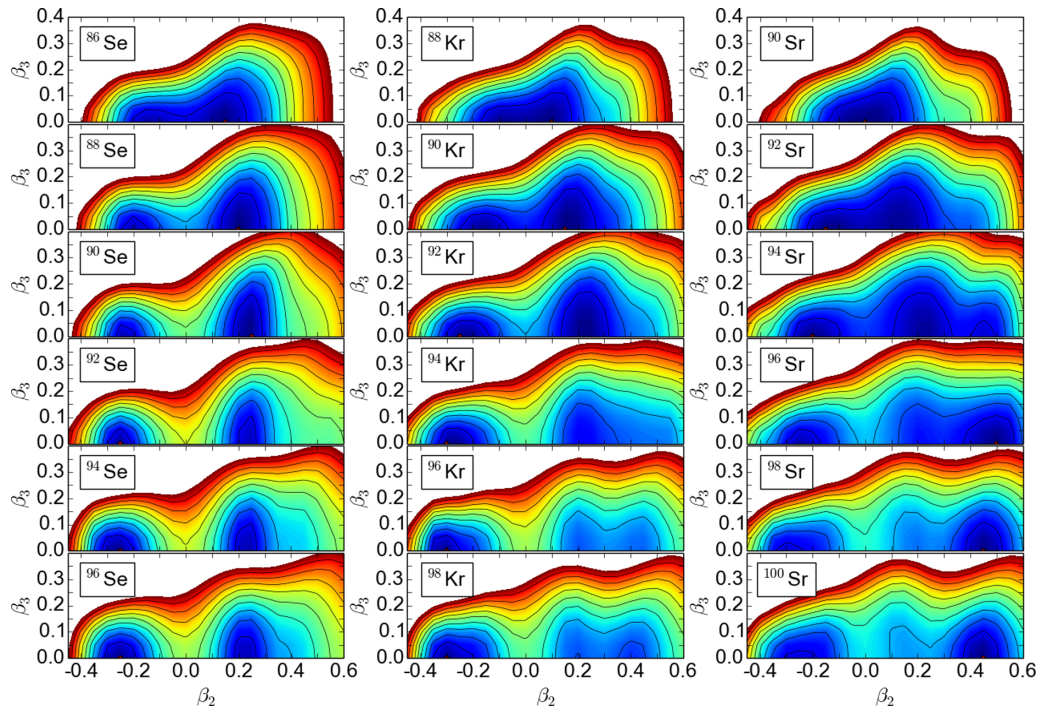


FIG. 3. Same as in the caption to Fig. 1 but for the neutron-rich nuclei  $^{86-96}\text{Se}$ ,  $^{88-98}\text{Kr}$ , and  $^{90-100}\text{Sr}$ .

example  $^{96,98}\text{Kr}$ , one notices two shallow local minima on the prolate side. For many nuclei in this region a number of both microscopic and empirical studies point to the presence of shape coexistence and/or  $\gamma$ -soft shapes. The present calculation is restricted to only axially symmetric shapes and, thus, a more realistic analysis should take into account the triaxial degrees of freedom.

#### D. $N = 56$ isotones

To analyze the evolution of the empirical  $N = 56$  octupole magic number, we performed constrained SCMF calculations along the isotonic chain  $N = 56$ . Figure 4 displays the resulting  $\beta_2$ - $\beta_3$  PESs for the  $N = 56$  even-even isotones from  $Z = 34$  ( $^{90}\text{Se}$ ) to  $Z = 56$  ( $^{112}\text{Ba}$ ). In the  $(\beta_2, \beta_3)$  PESs, neither an octupole-deformed equilibrium state nor octupole-soft potential is observed below the proton magic number  $Z = 50$ . For  $N = 56$  isotones beyond Sn, however, the potentials start to become more rigid in  $\beta_2$  and softer in  $\beta_3$ . Among the  $N = 56$  isotones depicted in the figure, the most pronounced octupole minimum is obtained for the nucleus  $^{112}\text{Ba}$  with  $N = Z = 56$ .

## IV. SPECTROSCOPIC RESULTS

In the following we present QOCH results for the spectroscopic properties relevant to quadrupole and octupole collective excitations. Note that the calculation also includes  $N \approx Z \approx 56$  nuclei that are close to the proton drip line. For these nuclei only very limited experimental information is available: the lightest known Xe, Ba, and Ce isotopes are  $^{110}\text{Xe}$ ,  $^{114}\text{Ba}$  [12], and  $^{118}\text{Ce}$ . For completeness, and

considering the signatures of octupole correlations on the corresponding  $(\beta_2, \beta_3)$  PESs in Fig. 1, we also discuss the spectroscopy of proton drip-line nuclei.

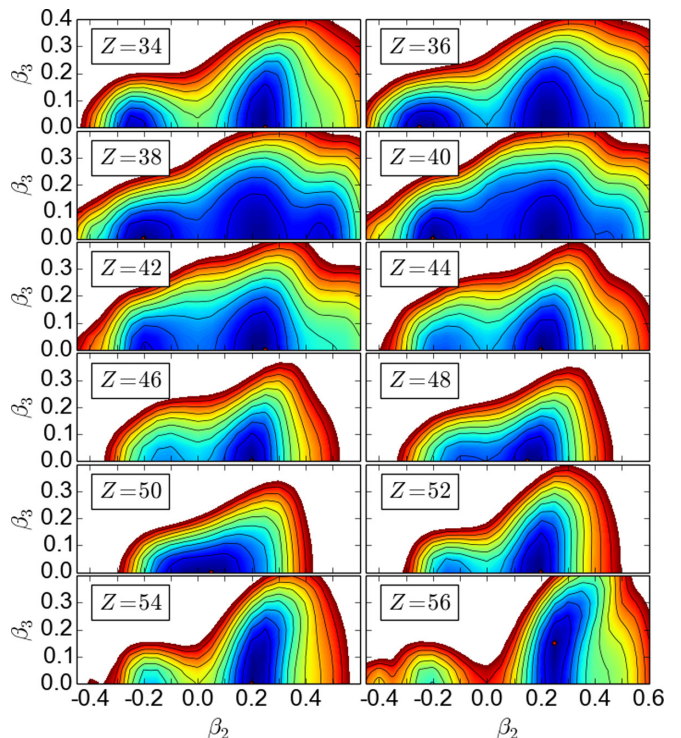


FIG. 4. Same as in the caption to Fig. 1 but for the  $N = 56$  isotones from  $^{90}\text{Se}$  ( $Z = 34$ ) to  $^{112}\text{Ba}$  ( $Z = 56$ ).

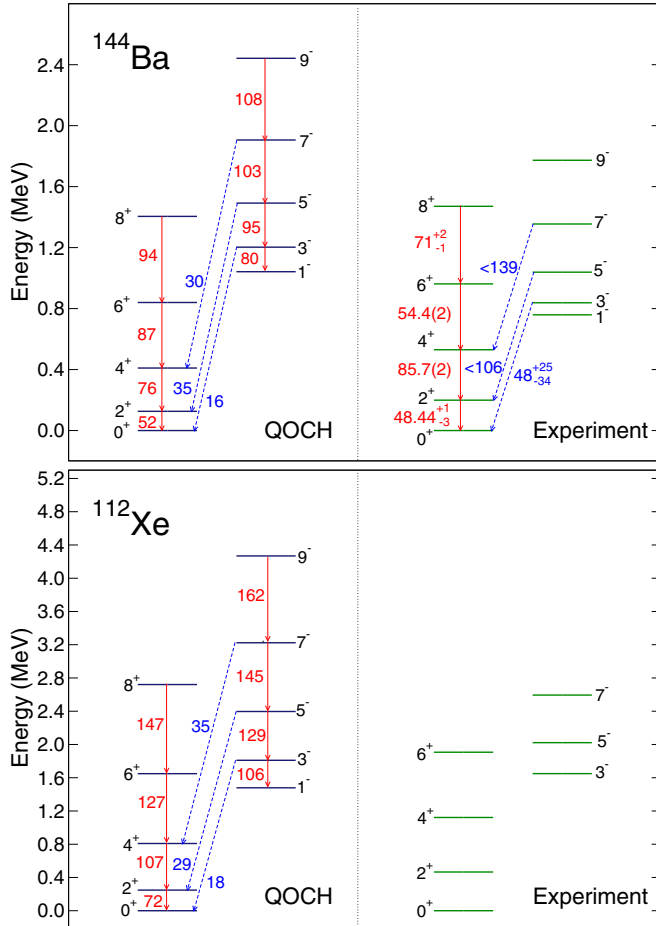


FIG. 5. Comparison of the QOCH and experimental low-energy excitation spectra for the positive- and negative-parity yrast states of  $^{144}\text{Ba}$  and  $^{112}\text{Xe}$ . Solid and dashed arrows denote  $E2$  and  $E3$  transitions, respectively, and the corresponding  $B(E2)$  and  $B(E3)$  values are given in Weisskopf units. Experimental results are from Refs. [6,51].

### A. Benchmark calculation: $^{144}\text{Ba}$ and $^{112}\text{Xe}$

As a test case, we consider the QOCH results for the low-energy positive-parity ( $\pi = +1$ ) and negative-parity ( $\pi = -1$ ) bands of  $^{144}\text{Ba}$  and  $^{112}\text{Xe}$ . These nuclei are specifically considered here as representative of the regions close to the neutron octupole magic numbers  $N \approx 88$  and  $56$ . In particular, recent experiments performed at the Argonne National Laboratory [6,7] have indicated that the neutron-rich nucleus  $^{144}\text{Ba}$  and neighboring Ba isotopes are characterized by pronounced ground-state octupole deformations. In Fig. 5 we compare the lowest  $\pi = +1$  and  $\pi = -1$  QOCH bands of  $^{144}\text{Ba}$  and  $^{112}\text{Xe}$  to the available data [6,51]. The predicted bands with both parities obtained from the present model calculation are in a reasonable agreement with the experimental ones. The model also reproduces the data on  $E2$  transitions in the  $\pi = +1$  band of  $^{144}\text{Ba}$ , and predicts  $B(E3)$  values for transitions between the  $\pi = +1$  and  $\pi = -1$  bands. In  $^{144}\text{Ba}$  the calculated  $B(E3; 3_1^- \rightarrow 0_1^+)$  value of 16 W.u. is within the range of experimental uncertainty. Previous GCM calculations for  $^{144}\text{Ba}$  based on the Gogny-D1S EDF provide [40,41] both positive-

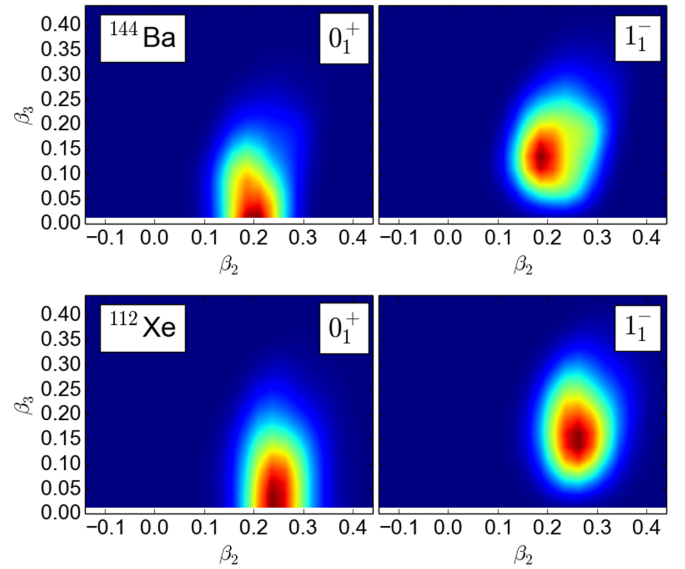


FIG. 6. Probability density distributions for the lowest positive-parity ( $0_1^+$ ) and negative-parity ( $1_1^-$ ) states of  $^{144}\text{Ba}$  (upper) and  $^{112}\text{Xe}$  (lower) in the  $\beta_2$ - $\beta_3$  plane.

and negative-parity bands that are stretched as compared to the experimental data, while the energy of the bandhead state  $1_1^-$  is accurately reproduced. Moreover, the  $B(E3; 3_1^- \rightarrow 0_1^+)$  transition rates of  $^{144}\text{Ba}$  predicted by the recent GCM calculations with both the Gogny-D1S EDF [40] and the relativistic functional PC-PK1 [42] are more or less similar to the one obtained in the present calculation. In the neutron-deficient  $N \approx Z \approx 56$  region,  $^{112}\text{Xe}$  is the lightest nucleus for which experimental information is available. The theoretical excitation spectrum is in qualitative agreement with the data, though we note that the calculated  $\pi = +1$  band appears to be somewhat more compressed than the experimental one.

Figure 6 plots the probability density distributions  $\rho_\alpha^{I\pi}(\beta_2, \beta_3)$  (14) of the lowest energy positive- ( $0_1^+$ ) and negative-parity ( $1_1^-$ ) states in the  $(\beta_2, \beta_3)$ -deformation space. One notices that, for both nuclei, the ground state  $0_1^+$  probability density is peaked at  $\beta_2 \approx \beta_{2,\text{min}}$ , where the global minimum occurs on the PES, and  $\beta_3 \approx 0$ . The collective wave functions for the  $1_1^-$  state are, however, concentrated at the same values of  $\beta_2$  as the corresponding ground states, but at finite values of the octupole deformation  $\beta_3 \approx 0.1$ – $0.15$ .

### B. Low-energy excitation spectra

The calculated excitation spectra for both even-spin positive-parity and odd-spin negative-parity yrast states are shown in Figs. 7 and 8, respectively, for the Xe, Ba, and Ce isotopic chains in comparison with available data. The theoretical positive-parity states are in good agreement with experimental results (Fig. 7), with the exception of nuclei in the immediate vicinity of the neutron magic number  $N = 82$ . For these nuclei the purely collective states of the QOCH cannot reproduce the empirical excitation spectrum on a quantitative level. Within the present calculation, the positive-parity bands in the three isotopic chains

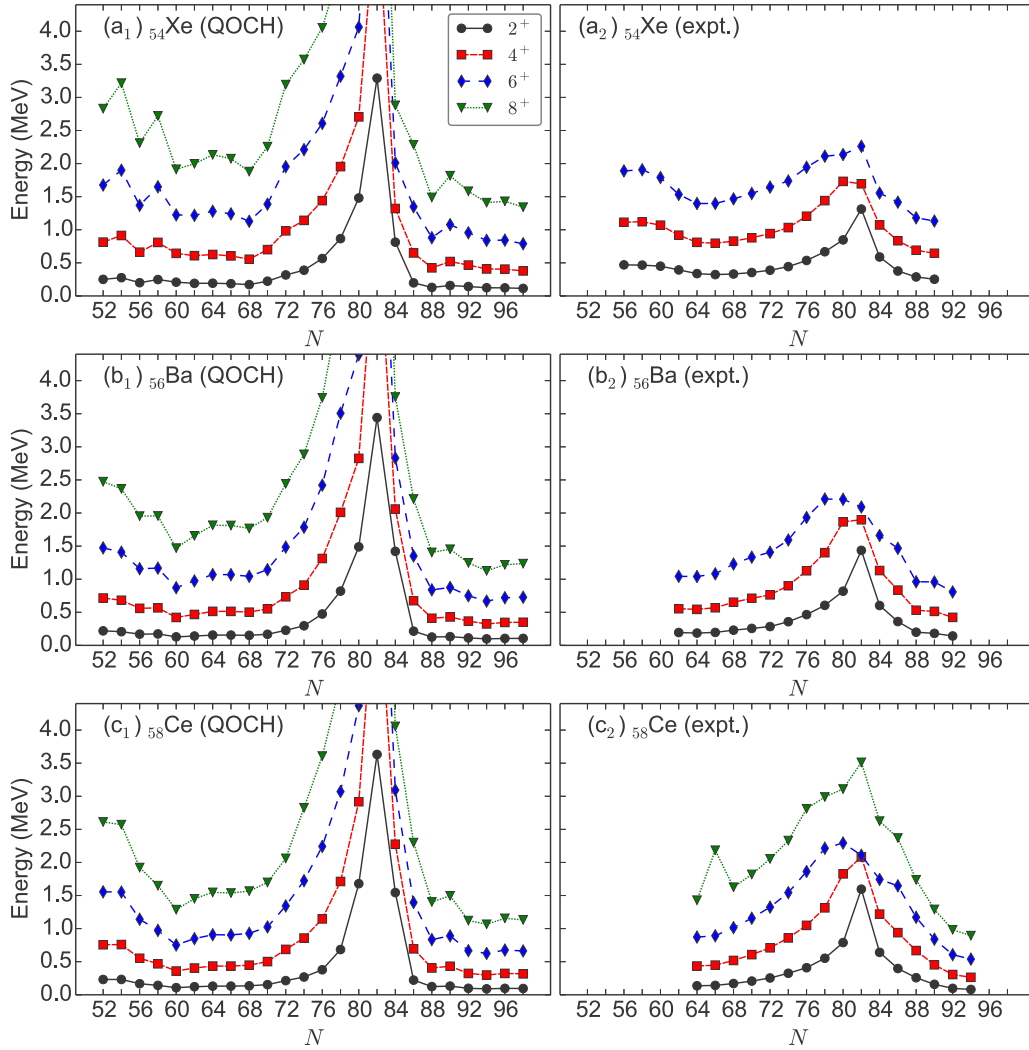


FIG. 7. Evolution of QOCH excitation spectra for the positive-parity yrast states along the chains of Xe, Ba, and Ce isotopes. Experimental values are from the ENSDF database [51].

are somewhat compressed as compared to the experimental values for  $52 \leq N \leq 72$  and  $N \geq 86$ . This reflects the fact that the SCMF potential surfaces for the corresponding nuclei exhibit more pronounced  $\beta_2$  deformations (Figs. 1 and 2). In addition, there is a noticeable staggering pattern of the predicted  $6_1^+$  and  $8_1^+$  excitation energies around  $N = 56$ , in particular, in the Xe isotopes [Fig. 1(a<sub>1</sub>)]. As seen from the SCMF results in Fig. 1, the topology of the PES varies rather rapidly from  $^{110}\text{Xe}$  to  $^{114}\text{Xe}$ ; that is, the degree of  $\beta_2$  softness increases. As a consequence, structures of the resultant positive-parity states could be significantly different between neighboring isotopes.

The results for the negative-parity states, shown in Fig. 8, are more interesting. The calculated levels for each isotopic chain exhibit evident signatures of enhanced octupole collectivity, that is, a parabolic behavior of excitation energies with neutron number, centered at around  $N \approx 56$  and  $N \approx 88$ . At these neutron numbers the levels become lowest in energy. This is consistent with the observed trend of the SCMF ( $\beta_2, \beta_3$ ) PESs in Figs. 1 and 2: in most of the nuclei around  $N = 56$  and  $88$  the corresponding PESs display global minima

at nonzero  $\beta_3$ . A marked difference between the predicted and experimental  $\pi = -1$  spectra is that the former increase rapidly as the neutron major shell  $N = 82$  is approached, while the latter shows a flatter behavior. Moreover, the quantitative agreement is not satisfactory for the  $J = 3^-, 5^-$ , and  $7^-$  excitation energies. As already mentioned, such discrepancies occur mainly because the present QOCH framework only deals with the collective states. Particularly for the low-lying negative-parity states in those nuclei near the magic numbers, noncollective degrees of freedom come to play a more relevant role. In such a case, phenomena like octupole vibrations of spherical shape emerge, but they cannot be fully accounted for within the present approach.

In Figs. 9 and 10 we display the QOCH results for the excitation energies of the lowest positive- and negative-parity states in neutron-rich Se, Kr, and Sr isotopes, respectively. There are only few tentative assignments of negative-parity states in neutron-rich  $Z = 34, 36, 38$  isotopes. Only few data for Kr isotopes are available. Also in this case one notices a kind of parabolic behavior centered at  $N = 56$ , but much less pronounced than in the proton-rich Xe, Ba, and Ce nuclei.

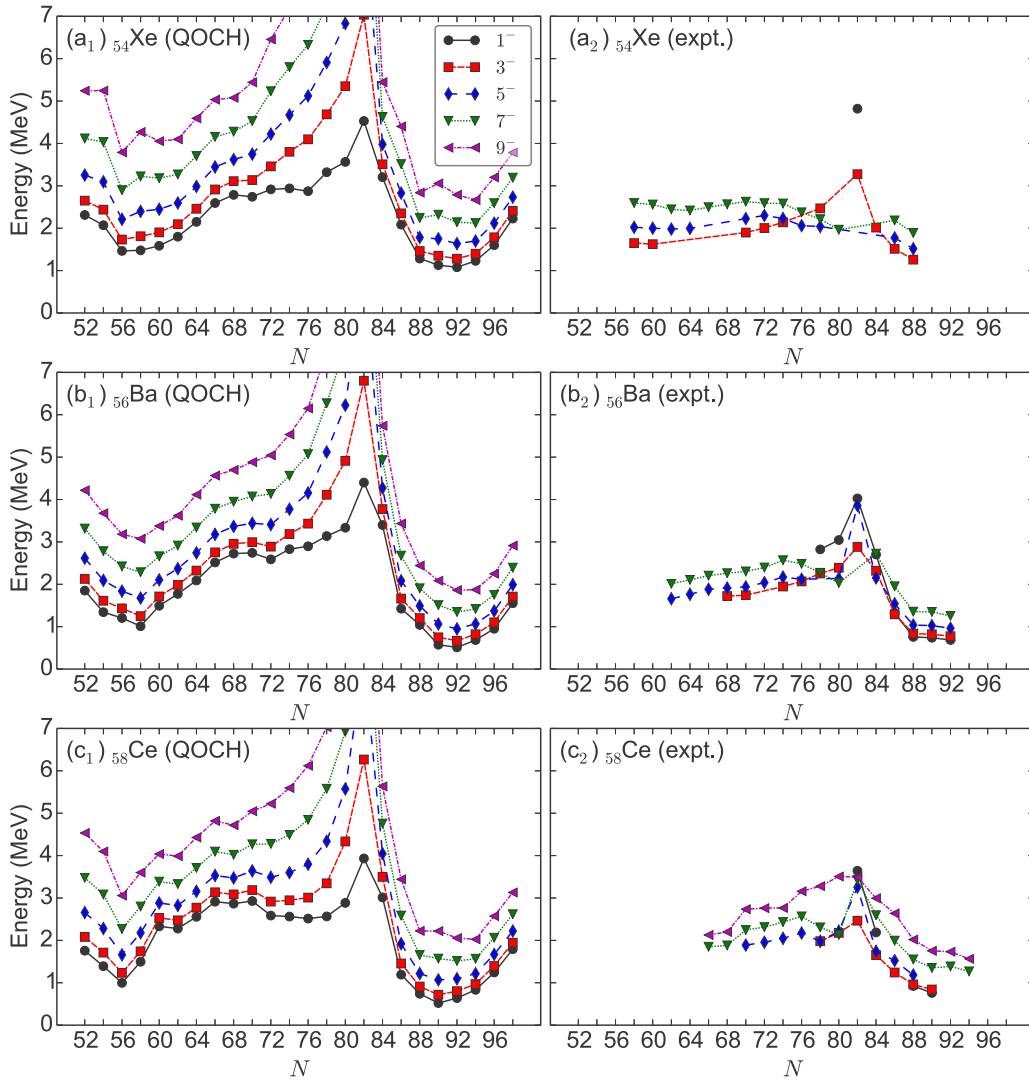


FIG. 8. Same as in the caption to Fig. 7 but for the negative-parity states.

Obviously in the latter case the  $Z \approx 56$  proton and  $N = 56$  numbers reinforce octupole correlations, and global minima at nonzero  $\beta_3$  are predicted. This does occur for the neutron-rich Se, Kr, and Sr isotopes, for which the corresponding PESs are at most soft in the  $\beta_3$  collective coordinates, as shown in Fig. 3. In fact, it is well known that for these nuclei it is far more important to include the triaxial degree of freedom in order to describe the excitation spectra at a quantitative level, and especially the shape transition at  $N = 60$ . A number of previous empirical and microscopic studies have confirmed that the effects of triaxial deformations and coexistence of different equilibrium shapes play an important role in determining the low-energy nuclear structure around  $N \approx 60$ . The present version of the QOCH model is restricted to axially symmetric shapes and, therefore, the calculated positive-parity spectra can only qualitatively reproduce the empirical isotopic trend (Fig. 9). Similarly to the experimental trend, the predicted positive-parity levels decrease as functions of  $N$ . The experimental data for the considered Se and Kr isotopes are reasonably described, except for the nearly spherical nucleus  $^{88}\text{Kr}$  ( $N = 52$ ). Note that especially in Sr isotopes

[Fig. 9(a<sub>2</sub>)] the experimental  $\pi = +1$  spectra show a marked peak at  $N = 56$ . This points to the  $N = 56$  neutron subshell closure due to filling of the  $2d_{5/2}$  orbital. This systematic is not observed in the predicted spectra. This is expected from the fact that the corresponding SCMF  $\beta_2$ - $\beta_3$  map for  $^{94}\text{Sr}$  is well deformed (Fig. 3).

### C. Electromagnetic properties

The results for the  $B(E2; 2_1^+ \rightarrow 0_1^+)$ ,  $B(E3; 3_1^- \rightarrow 0_1^+)$ , and  $B(E1; 1_1^- \rightarrow 0_1^+)$  reduced transition probabilities along the Xe, Ba, and Ce isotopic chains are shown in Fig. 11. We note a reasonable agreement with the experimental  $B(E2)$  values, especially considering that bare charges are used in the calculation. Much less information is available on the  $B(E3)$  values. What is interesting is that the theoretical  $B(E3)$  values exhibit two peaks, one at  $N \approx 56$  and the other at  $N \approx 88$ . These neutron numbers, of course, correspond to the ones at which octupole collectivity is most enhanced. Considering the results on a more quantitative level, in each isotopic chain the QOCH results for the  $B(E3)$  rates systematically

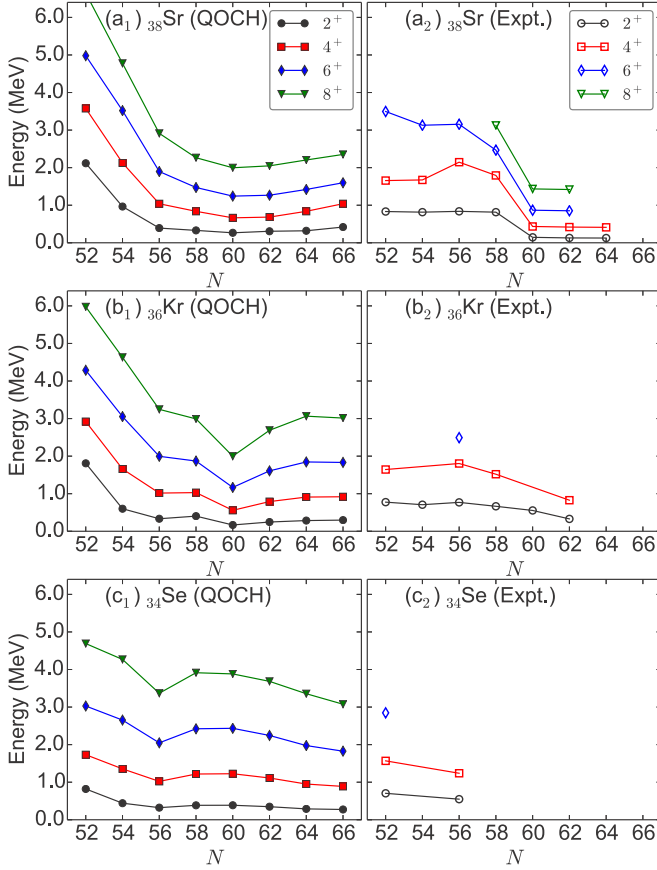


FIG. 9. Same as in the caption to Fig. 7 but for the positive-parity states in Se, Kr, and Sr isotopes.

underestimate the experimental values. The exceptions are  $^{144,146}\text{Ba}$ , for which the experimental values are characterized by large uncertainties (see also Fig. 5). The reason why the QOCH cannot quantitatively reproduce the experimental  $B(E3)$  values is probably because of the fact that, for those nuclei that are close to the neutron magic number  $N = 82$ , the calculated energies of the  $3^-$  state are also not in a particularly good agreement with experimental results (cf. Fig. 8). As shown in Fig. 2, for those nuclei that are nearly spherical, there is no octupole deformation or octupole softness at the SCMF level, so the collective model is not expected to provide a very good description of  $E3$  transition strength. There is no experimental information for the  $E1$  transition strengths. The systematics of the calculated  $B(E1)$  values exhibits certain peaks for particular nuclei, but they are not necessarily the same as for the  $B(E3)$  values. The  $E1$  transitions are less collective in nature compared to the  $E2$  and  $E3$  ones; hence the collective model does not necessarily provide accurate predictions for the  $B(E1)$  values.

## V. SYSTEMATICS ALONG THE $N = 56$ ISOTONIC CHAINS

We also explored the systematics of excitation energies along the  $N = 56$  isotones. The QOCH results for the low-energy positive-parity and negative-parity spectra are shown in Fig. 12. The predicted positive-parity levels remain almost

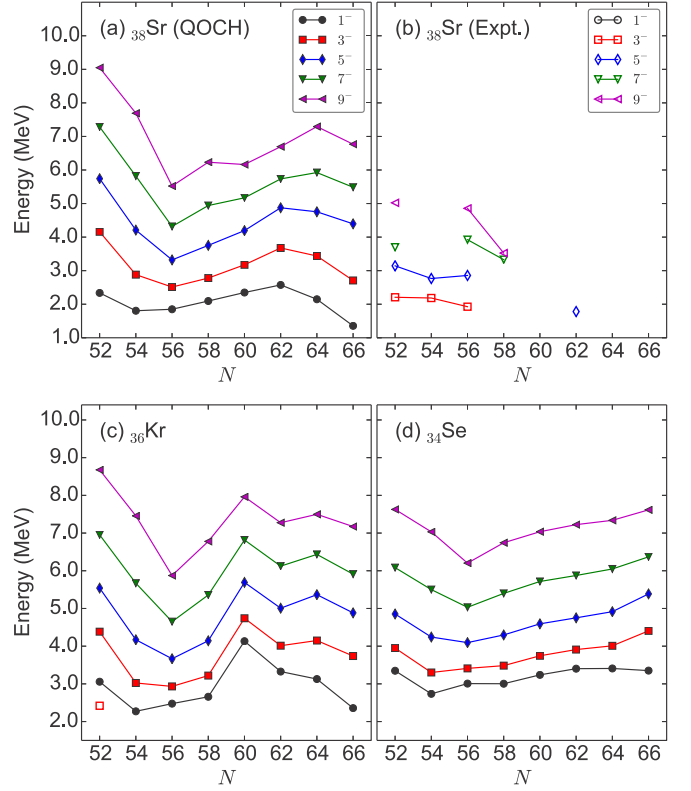


FIG. 10. Same as in the caption to Fig. 7 but for the negative-parity states in Se, Kr, and Sr isotopes.

constant with proton number  $Z$ , except for the  $Z = 50$  shell closure. The model qualitatively reproduces the corresponding experimental  $\pi = +1$  spectra, with the exception of a pronounced proton-number dependence observed in the region  $36 \leq Z \leq 42$ . The cusp in the experimental yrast states indicates the  $Z = 40$  proton subshell closure, which is not properly accounted for in the present calculation restricted to axial symmetry. The failure in describing this experimental pattern could also be attributed to the fact that both the employed energy density functional and pairing property are not specifically adjusted to reproduce the  $Z = 40$  subshell closure. The computed  $\pi = -1$  states become lowest in energy at  $Z \approx 40$  for the  $Z < 50$  region. Beyond the proton magic number  $Z = 50$ , level spacing between the negative-parity states is strongly reduced, and their energies display the parabolic trend characteristic of pronounced octupole correlations. The calculation also reproduces the empirical  $B(E2)$  values, but underestimates the two known  $B(E3; 3_1^- \rightarrow 0_1^+)$  at  $Z = 42$  and  $Z = 44$  by approximately a factor of 2.

## VI. SIGNATURES OF OCTUPOLE SHAPE TRANSITIONS

As signatures of quadrupole and octupole shape transitions, we plot in Fig. 13 the average values of the axial quadrupole  $\overline{\beta_2}$  [Fig. 13(a)] and  $\overline{\beta_3}$  [Fig. 13(b)] deformation parameters in the QOCH ground states  $0_1^+$ , and their fluctuations  $\delta\beta_2/\overline{\beta_2}$  and  $\delta\beta_3/\overline{\beta_3}$ , respectively, for the Ce, Ba, Xe, Sr, Kr, and Se isotopes, as functions of the neutron number. Here the average  $\overline{\beta_\lambda}$  ( $\lambda = 2, 3$ ) is defined as  $\overline{\beta_\lambda} = \sqrt{\langle \beta_\lambda^2 \rangle}$ , and

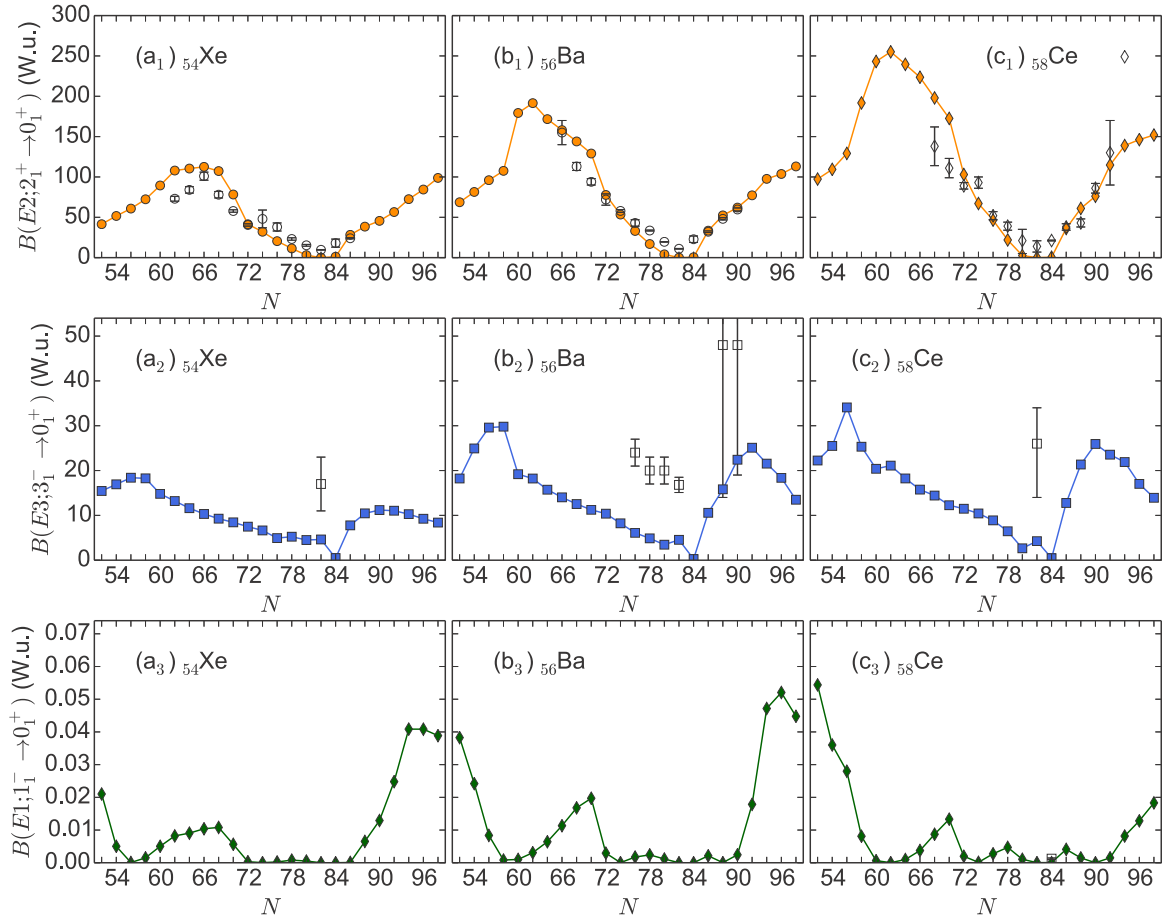


FIG. 11.  $B(E2; 2_1^+ \rightarrow 0_1^+)$  (top),  $B(E3; 3_1^- \rightarrow 0_1^+)$  (middle), and  $B(E1; 1_1^- \rightarrow 0_1^+)$  (bottom) reduced transition probabilities for the Xe, Ba, and Ce isotopes. Solid symbols connected by lines denote the QOCH results. Experimental values (open symbols) are taken from the ENSDF database [51].

$\delta\beta_\lambda$  denotes the variance  $\delta\beta_\lambda = \sqrt{\langle\beta_\lambda^4\rangle - \langle\beta_\lambda^2\rangle^2/2\bar{\beta}_\lambda}$  [52,53]. In Fig. 13(a), as expected from both the SCMF ( $\beta_2, \beta_3$ ) PESs and the calculated excitation spectra, the average deformation  $\bar{\beta}_2$  increases towards the middle of the major shell, as the quadrupole collectivity becomes larger. The octupole deformation  $\bar{\beta}_3$  exhibits a parabolic behavior in two regions, centered at the neutron numbers  $N = 56$  and  $88$ , at which it reaches maximum values larger than  $\bar{\beta}_3 \approx 0.15$ .

In Fig. 13(c), fluctuations of the  $\beta_2$  deformation for the Se, Kr, and Sr isotopes change abruptly from  $N = 58$  to  $60$ . This reflects the rapid structural evolution in these nuclei, most noticeably in Kr, the relevant spectroscopic properties indicating phase-transitional behavior at  $N = 60$ . The fluctuations of  $\beta_2$  for the Xe, Ba, and Ce isotopes exhibit only a moderate change. This is consistent with the SCMF results that the minima are more rigid in  $\beta_2$ .

The fluctuation in octupole deformation  $\beta_3$ , depicted in Fig. 13(d), presents a measure for octupole softness. Especially for the Sr and Kr nuclei near  $N = 54$ – $56$ , and for the Ba and Ce nuclei from  $N = 88$  to  $90$ , we observe a marked discontinuity characteristic of octupole shape-phase transitions. The isotopic dependence of the fluctuation in

Fig. 13(d) correlates with the systematics of spectroscopic properties.

We note that in Fig. 13(a) the average  $\bar{\beta}_2$  has a finite value  $\approx 0.05$  for those Xe, Ba, and Ce nuclei near the magic number  $N = 82$ . This is at variance with the SCMF result, in which the equilibrium minimum is found at  $(\beta_2, \beta_3) \approx (0, 0)$  for the  $N \approx 82$  nuclei. However, the average  $\bar{\beta}_2$  is here obtained by using the wave functions resulting from the diagonalization of the QOCH and, therefore, does not necessarily coincide with the equilibrium minimum in the SCMF calculation. Similar results were obtained in a previous SCMF plus five-dimensional collective Hamiltonian approach [54]. We have also confirmed that the calculated  $0_1^+$  wave functions for the Ba isotopes with  $N = 80, 82$ , and  $84$  have the largest probability amplitudes at  $|\beta_2| \approx 0.05$ . Finally, the large  $\beta_2$  fluctuations at the  $N = 82$  magic number are due to vanishing values of  $\bar{\beta}_2$  in the denominator in spherical nuclei.

## VII. CONCLUSIONS

Octupole collective excitations were analyzed using the fully microscopic framework of nuclear density functional theory. Axially symmetric quadrupole-octupole constrained

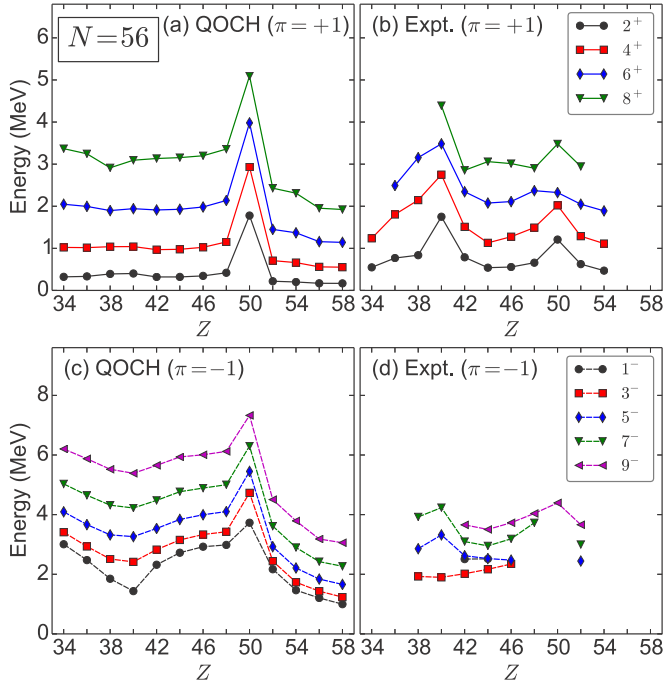


FIG. 12. Excitation spectra of the low-lying positive- (top row) and negative-parity (bottom row) yrast states of the  $N = 56$  isotones as functions of the proton number  $Z$ . The excitation spectra computed with the QOCH are plotted on the left-hand side of the figure, and are compared with the available experimental data [51] on the right.

SCMF calculations based on a choice of universal energy density functional and pairing interaction were performed in three mass regions of the nuclear chart in which enhanced octupole correlations are empirically expected to occur: neutron-deficient nuclei with  $Z \approx 56$  and  $N \approx 56$ , neutron-rich nuclei with  $Z \approx 56$  and  $N \approx 88$ , and the neutron-rich nuclei with  $Z \approx 34$  and  $N \approx 56$ . The resulting potential energy surfaces in the  $(\beta_2, \beta_3)$  plane indicate octupole-deformed equilibrium states at the SCMF level in  $^{112,114}\text{Ba}$  and  $^{114}\text{Ce}$  on the neutron-deficient side, and in a number of neutron-rich Ba and Ce nuclei around  $N = 88$ .

The SCMF calculations completely determine the ingredients of the quadrupole-octupole collective Hamiltonian: the moment of inertia, three mass parameters, and the collective potential. The diagonalization of the QOCH subsequently yields the positive- and negative-parity excitation spectra and the electric quadrupole, octupole, and dipole transition strengths that are relevant to the quadrupole and octupole modes of collective excitations. The predicted excitation spectra for both parities and the  $B(E2)$  and  $B(E3)$  values of the neutron-deficient and neutron-rich  $Z \approx 56$  nuclei are in a reasonable agreement with the experimental data. These quantities indicate a parabolic systematics around the neutron numbers  $N = 56$  and  $88$ , at which the SCMF  $(\beta_2, \beta_3)$  PESs exhibit pronounced octupole-deformed minima. The calculated spectroscopic properties for the neutron-rich nuclei with  $Z \approx 34$  and  $N \approx 56$  also indicate a signature of enhanced octupole collectivity around  $N \approx 56$ , though not as distinct as

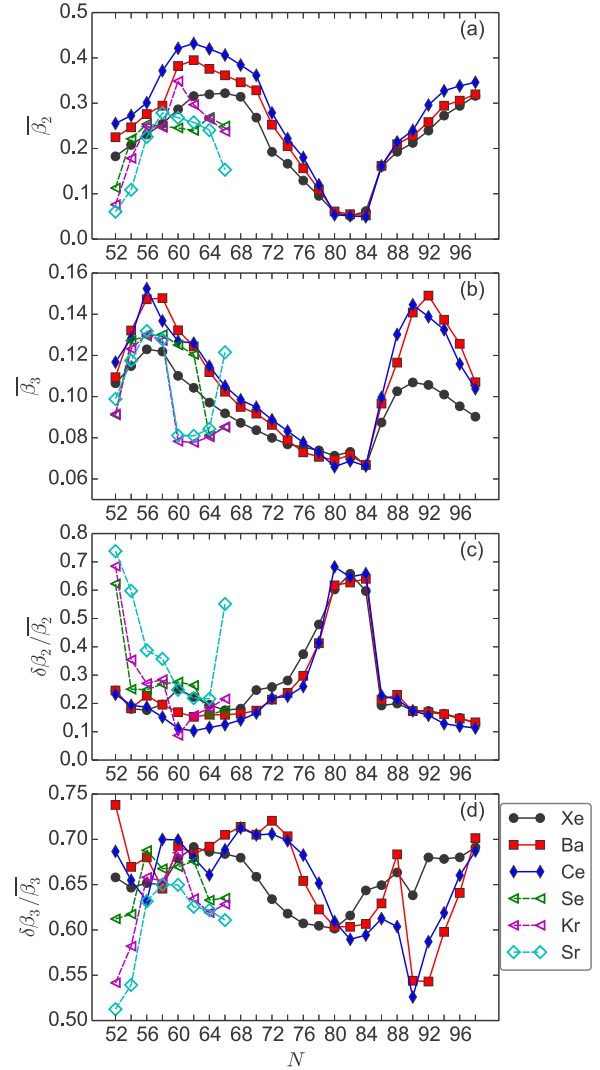


FIG. 13. Average values of the (a)  $\beta_2$  and (b)  $\beta_3$  deformation parameters in the  $0_1^+$  ground state,  $\overline{\beta}_\lambda = \sqrt{\langle \beta_\lambda^2 \rangle}$ , and the fluctuations (c)  $\delta\beta_2/\overline{\beta}_2$  and (d)  $\delta\beta_3/\overline{\beta}_3$ , for the Xe, Ba, Ce, Se, Kr, and Sr isotopes as functions of the neutron number  $N$ . The variance  $\delta\beta_\lambda$  is defined as  $\delta\beta_\lambda = \sqrt{\langle \beta_\lambda^4 \rangle - \langle \beta_\lambda^2 \rangle^2} / 2\overline{\beta}_\lambda$ .

in the case of the  $Z \approx 56$  isotopes. We further explored spectroscopic properties along the  $N = 56$  isotones, from  $Z = 34$  to 58. The relevant quantities, i.e., negative-parity spectra and  $B(E3)$  transitions, again point to an enhancement of octupole correlations around  $Z = 34$  and 56. In general, octupole collectivity appears to be more enhanced in the  $N \approx 88$  region than around  $N \approx 56$ . The present fully microscopic spectroscopic calculation has predicted several nuclei with stable octupole deformation in the neutron-deficient  $Z \approx 56$  nuclei that have not been investigated so far. The average  $\beta_2$  and  $\beta_3$  deformations calculated in the QOCH ground states, as well as their fluctuations, exhibit signatures of quadrupole and octupole shape-phase transitions.

The current implementation of the QOCH method is restricted to axially symmetric shapes. Hence some discrepancies with the experimental spectroscopic properties could

be traced back to this limitation. In particular, the fact that the positive-parity states for the neutron-rich  $Z \approx 34$  and  $N \approx 56$  nuclei have not been reproduced quantitatively indicates that triaxial shape degrees of freedom need to be included as additional collective coordinates. This requires the inclusion of several new terms in the collective Schrödinger equation, but in practical applications such an extension would be very complicated. Thus, a method that consists in mapping the SCMF solutions onto the interacting-boson Hamiltonian [55] could be more feasible for the inclusion of triaxial degrees of freedom. Work in this direction presents an interesting future study.

## ACKNOWLEDGMENTS

This work has been supported by the Tenure Track Pilot Programme of the Croatian Science Foundation and the École Polytechnique Fédérale de Lausanne, and the Project No. TTP-2018-07-3554 Exotic Nuclear Structure and Dynamics, with funds of the Croatian-Swiss Research Programme. It has also been supported in part by the QuantiXLie Centre of Excellence, a project co-financed by the Croatian Government and European Union through the European Regional Development Fund, the Competitiveness and Cohesion Operational Programme (KK.01.1.1.01.0004).

- 
- [1] P. A. Butler and W. Nazarewicz, *Rev. Mod. Phys.* **68**, 349 (1996).
- [2] P. A. Butler, *J. Phys. G: Nucl. Part. Phys.* **43**, 073002 (2016).
- [3] L. P. Gaffney, P. A. Butler, M. Scheck, A. B. Hayes, F. Wenander, M. Albers, B. Bastin, C. Bauer, A. Blazhev, S. Bönig, N. Bree, J. Cederkäll, T. Chupp, D. Cline, T. E. Cocolios, T. Davinson, H. D. Witte, J. Diriken, T. Grahn, A. Herzan *et al.*, *Nature (London)* **497**, 199 (2013).
- [4] P. A. Butler, L. P. Gaffney, P. Spagnoletti, K. Abrahams, M. Bowry, J. Cederkäll, G. de Angelis, H. De Witte, P. E. Garrett, A. Goldkuhle, C. Henrich, A. Illana, K. Johnston, D. T. Joss, J. M. Keatings, N. A. Kelly, M. Komorowska, J. Konki, T. Kröll, M. Lozano *et al.*, *Phys. Rev. Lett.* **124**, 042503 (2020).
- [5] M. M. R. Chishti, D. O'Donnell, G. Battaglia, M. Bowry, D. A. Jaroszynski, B. S. N. Singh, M. Scheck, P. Spagnoletti, and J. F. Smith, *Nat. Phys.* **16**, 853 (2020).
- [6] B. Bucher, S. Zhu, C. Y. Wu, R. V. F. Janssens, D. Cline, A. B. Hayes, M. Albers, A. D. Ayangeakaa, P. A. Butler, C. M. Campbell, M. P. Carpenter, C. J. Chiara, J. A. Clark, H. L. Crawford, M. Cromaz, H. M. David, C. Dickerson, E. T. Gregor, J. Harker, C. R. Hoffman *et al.*, *Phys. Rev. Lett.* **116**, 112503 (2016).
- [7] B. Bucher, S. Zhu, C. Y. Wu, R. V. F. Janssens, R. N. Bernard, L. M. Robledo, T. R. Rodríguez, D. Cline, A. B. Hayes, A. D. Ayangeakaa, M. Q. Buckner, C. M. Campbell, M. P. Carpenter, J. A. Clark, H. L. Crawford, H. M. David, C. Dickerson, J. Harker, C. R. Hoffman, B. P. Kay *et al.*, *Phys. Rev. Lett.* **118**, 152504 (2017).
- [8] S. L. Rugari, R. H. France, B. J. Lund, Z. Zhao, M. Gai, P. A. Butler, V. A. Holliday, A. N. James, G. D. Jones, R. J. Poynter, R. J. Tanner, K. L. Ying, and J. Simpson, *Phys. Rev. C* **48**, 2078 (1993).
- [9] C. Fahlander, D. Seweryniak, J. Nyberg, Z. Dombrádi, G. Perez, M. Józsa, B. Nyakó, A. Atac, B. Cederwall, A. Johnson, A. Kerek, J. Kownacki, L.-O. Norlin, R. Wyss, E. Adamides, E. Ideguchi, R. Julin, S. Juutinen, W. Karczmarczyk, S. Mitarai *et al.*, *Nucl. Phys. A* **577**, 773 (1994).
- [10] J. F. Smith, C. J. Chiara, D. B. Fossan, G. J. Lane, J. M. Sears, I. Thorslund, H. Amro, C. N. Davids, R. V. F. Janssens, D. Seweryniak, I. M. Hibbert, R. Wadsworth, I. Y. Lee, and A. O. Macchiavelli, *Phys. Rev. C* **57**, R1037 (1998).
- [11] J. Smith, C. Chiara, D. Fossan, D. LaFosse, G. Lane, J. Sears, K. Starosta, M. Devlin, F. Lerma, D. Sarantites, S. Freeman, M. Leddy, J. Durell, A. Boston, E. Paul, A. Semple, I. Lee, A. Macchiavelli, and P. Heenen, *Phys. Lett. B* **523**, 13 (2001).
- [12] L. Capponi, J. F. Smith, P. Ruotsalainen, C. Scholey, P. Rakhila, K. Auranen, L. Bianco, A. J. Boston, H. C. Boston, D. M. Cullen, X. Derkx, M. C. Drummond, T. Grahn, P. T. Greenlees, L. Grocutt, B. Hadinia, U. Jakobsson, D. T. Joss, R. Julin, S. Juutinen *et al.*, *Phys. Rev. C* **94**, 024314 (2016).
- [13] T. Rzaca-Urban, W. Urban, A. Kaczor, J. L. Durell, M. J. Leddy, M. A. Jones, W. R. Phillips, A. G. Smith, B. J. Varley, I. Ahmad, L. R. Morss, M. Bentaleb, E. Lubkiewicz, and N. Schulz, *Eur. Phys. J. A* **9**, 165 (2000).
- [14] E. T. Gregor, M. Scheck, R. Chapman, L. P. Gaffney, J. Keatings, K. R. Mashtakov, D. O'Donnell, J. F. Smith, P. Spagnoletti, M. Thürauf, V. Werner, and C. Wiseman, *Eur. Phys. J. A* **53**, 50 (2017).
- [15] W. Nazarewicz, P. Olanders, I. Ragnarsson, J. Dudek, G. A. Leander, P. Möller, and E. Ruchowska, *Nucl. Phys. A* **429**, 269 (1984).
- [16] S. Y. Xia, H. Tao, Y. Lu, Z. P. Li, T. Nikšić, and D. Vretenar, *Phys. Rev. C* **96**, 054303 (2017).
- [17] S. E. Agbemava, A. V. Afanasjev, and P. Ring, *Phys. Rev. C* **93**, 044304 (2016).
- [18] S. E. Agbemava and A. V. Afanasjev, *Phys. Rev. C* **96**, 024301 (2017).
- [19] Y. Cao, S. E. Agbemava, A. V. Afanasjev, W. Nazarewicz, and E. Olsen, *Phys. Rev. C* **102**, 024311 (2020).
- [20] J. Engel and F. Iachello, *Nucl. Phys. A* **472**, 61 (1987).
- [21] N. V. Zamfir and D. Kusnezov, *Phys. Rev. C* **63**, 054306 (2001).
- [22] N. V. Zamfir and D. Kusnezov, *Phys. Rev. C* **67**, 014305 (2003).
- [23] K. Nomura, D. Vretenar, and B.-N. Lu, *Phys. Rev. C* **88**, 021303(R) (2013).
- [24] K. Nomura, D. Vretenar, T. Nikšić, and B.-N. Lu, *Phys. Rev. C* **89**, 024312 (2014).
- [25] P. G. Bizzeti and A. M. Bizzeti-Sona, *Phys. Rev. C* **88**, 011305(R) (2013).
- [26] D. Bonatsos, A. Martinou, N. Minkov, S. Karampagia, and D. Petrellis, *Phys. Rev. C* **91**, 054315 (2015).
- [27] T. M. Shneidman, G. G. Adamian, N. V. Antonenko, R. V. Jolos, and W. Scheid, *Phys. Lett. B* **526**, 322 (2002).
- [28] T. M. Shneidman, G. G. Adamian, N. V. Antonenko, R. V. Jolos, and W. Scheid, *Phys. Rev. C* **67**, 014313 (2003).
- [29] J. Skalski, *Phys. Lett. B* **238**, 6 (1990).
- [30] T. H. R. Skyrme, *Nucl. Phys.* **9**, 615 (1958).
- [31] P.-H. Heenen, J. Skalski, P. Bonche, and H. Flocard, *Phys. Rev. C* **50**, 802 (1994).
- [32] M. Bender, P.-H. Heenen, and P.-G. Reinhard, *Rev. Mod. Phys.* **75**, 121 (2003).

- [33] J. Erler, P. Klüpfel, and P.-G. Reinhard, *J. Phys. G: Nucl. Part. Phys.* **38**, 033101 (2011).
- [34] D. Vretenar, A. V. Afanasjev, G. A. Lalazissis, and P. Ring, *Phys. Rep.* **409**, 101 (2005).
- [35] T. Nikšić, D. Vretenar, and P. Ring, *Prog. Part. Nucl. Phys.* **66**, 519 (2011).
- [36] L. M. Robledo, T. R. Rodríguez, and R. R. Rodríguez-Guzmán, *J. Phys. G: Nucl. Part. Phys.* **46**, 013001 (2019).
- [37] P. Ring and P. Schuck, *The Nuclear Many-Body Problem* (Springer-Verlag, Berlin, 1980).
- [38] L. M. Robledo and P. A. Butler, *Phys. Rev. C* **88**, 051302(R) (2013).
- [39] J. M. Yao, E. F. Zhou, and Z. P. Li, *Phys. Rev. C* **92**, 041304(R) (2015).
- [40] R. N. Bernard, L. M. Robledo, and T. R. Rodríguez, *Phys. Rev. C* **93**, 061302(R) (2016).
- [41] R. Lică, G. Benzoni, T. R. Rodríguez, M. J. G. Borge, L. M. Fraile, H. Mach, A. I. Morales, M. Madurga, C. O. Sotty, V. Vedia, H. De Witte, J. Benito, R. N. Bernard, T. Berry, A. Bracco, F. Camera, S. Ceruti, V. Charviakova, N. Cieplicka-Oryńczak, C. Costache *et al.* (IDS Collaboration), *Phys. Rev. C* **97**, 024305 (2018).
- [42] Y. Fu, H. Wang, L.-J. Wang, and J. M. Yao, *Phys. Rev. C* **97**, 024338 (2018).
- [43] R. Rodríguez-Guzmán, Y. M. Humadi, and L. M. Robledo, *J. Phys. G: Nucl. Part. Phys.* **48**, 015103 (2020).
- [44] Z. P. Li, B. Y. Song, J. M. Yao, D. Vretenar, and J. Meng, *Phys. Lett. B* **726**, 866 (2013).
- [45] Z. Xu and Z.-P. Li, *Chin. Phys. C* **41**, 124107 (2017).
- [46] T. Nikšić, D. Vretenar, and P. Ring, *Phys. Rev. C* **78**, 034318 (2008).
- [47] Y. Tian, Z. Y. Ma, and P. Ring, *Phys. Lett. B* **676**, 44 (2009).
- [48] P. W. Zhao, Z. P. Li, J. M. Yao, and J. Meng, *Phys. Rev. C* **82**, 054319 (2010).
- [49] L. M. Robledo and G. F. Bertsch, *Phys. Rev. C* **84**, 054302 (2011).
- [50] L. M. Robledo, *J. Phys. G: Nucl. Part. Phys.* **42**, 055109 (2015).
- [51] Brookhaven National Nuclear Data Center, <http://www.nndc.bnl.gov>.
- [52] Z. P. Li, T. Nikšić, D. Vretenar, and J. Meng, *Phys. Rev. C* **81**, 034316 (2010).
- [53] J. Srebrny, T. Czosnyka, C. Droste, S. Rohoziński, L. Próchniak, K. Zajač, K. Pomorski, D. Cline, C. Wu, A. Bäcklin, L. Hasselgren, R. Diamond, D. Habs, H. Körner, F. Stephens, C. Baktash, and R. Kostecki, *Nucl. Phys. A* **766**, 25 (2006).
- [54] J. Xiang, Z. P. Li, W. H. Long, T. Nikšić, and D. Vretenar, *Phys. Rev. C* **98**, 054308 (2018).
- [55] K. Nomura, N. Shimizu, and T. Otsuka, *Phys. Rev. Lett.* **101**, 142501 (2008).